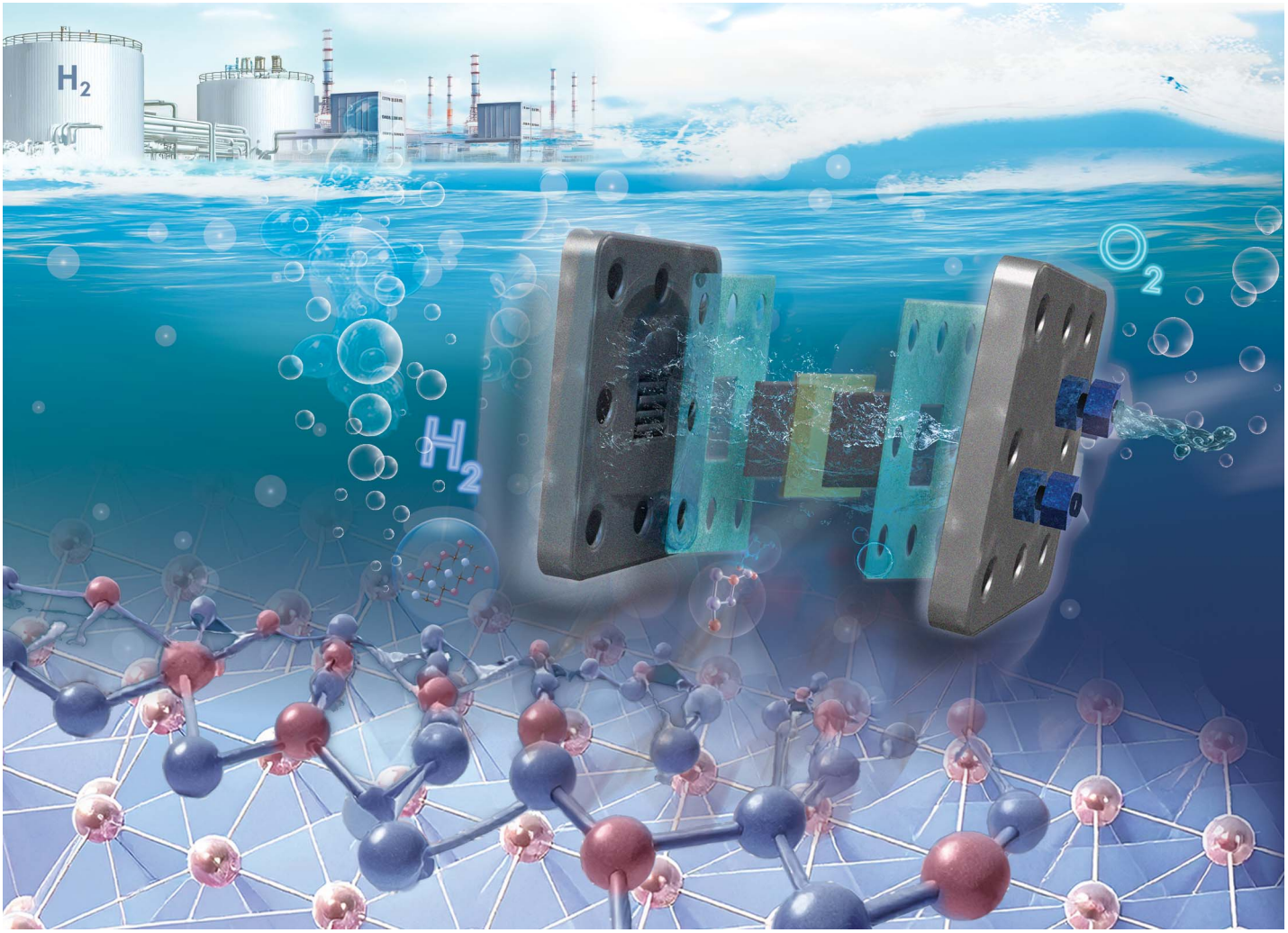

Showcasing a study on durable, noble-metal-free electrocatalysts for seawater splitting in AEM electrolyzers, by Professor Zdeněk Sofer's group (University of Chemistry and Technology, Prague, Czech Republic) with contributions from Professor Arkady V. Krasheninnikov's laboratory (Helmholtz-Zentrum Dresden-Rossendorf, Germany).

MXene-assisted CoZnCr for efficient alkaline seawater splitting and assembly of an anion exchange membrane electrolyzer

The cover art illustrates an AEM electrolyzer operating in alkaline seawater, producing hydrogen for industrial applications. A CoZnCr-LDH@Mo_2TiC_2-MXene heterostructure boosts charge transfer and suppresses chloride corrosion, highlighting a path toward scalable, sustainable hydrogen generation.

Image reproduced by permission of Zdeněk Sofer from *J. Mater. Chem. A,* 2025, **13**, 41752.

Cover image generated with AI.

As featured in:

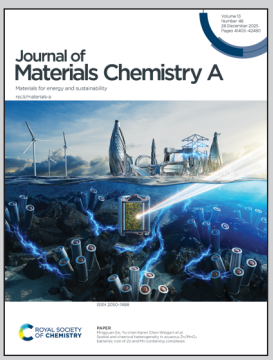

See Payal Chauhan, Zdeněk Sofer *et al.,* *J. Mater. Chem. A,* 2025, **13**, 41752.

ROYAL SOCIETY OF CHEMISTRY

rsc.li/materials-a

Registered charity number: 207890

Journal of Materials Chemistry A

ROYAL SOCIETY OF CHEMISTRY

PAPER

View Article Online
View Journal | View Issue

Cite this: J. Mater. Chem. A, 2025, 13, 41752

MXene-assisted CoZnCr for efficient alkaline seawater splitting and assembly of an anion exchange membrane electrolyzer†

Payal Chauhan,*[a] Prosun Santra,[b] Bing Wu,[a] Jan Plutnar,[a] Jakub Regner,[a] Alkesh B. Patel,[a] Martin Loula,[c] Mahdi Ghorbani-Asl,[b] Arkady V. Krasheninnikov,[b] Saeed Ashtiani,[a] Bahareh Khezri[def] and Zdeněk Sofer*[a]

Designing efficient electrocatalysts for industrial-scale seawater splitting that can mitigate anodic corrosion while effectively driving oxygen evolution remains a significant challenge. Strategic surface engineering is crucial in developing electrocatalysts, bridging the gap between fundamental research and the practical demands of industrial water-splitting applications. In this work, we present the development of a CoZnCr@MXene heterostructure, which achieves a low cell voltage of 1.55 V at a current density of 50 mA cm^{-2} and outperforms RuO_2 in alkaline seawater electrolyte. The remarkable performance is attributed to synergistic enhancements arising from compositional tuning, surface engineering, and the integration of conductive supports, which collectively lead to substantial reductions in overpotentials for the oxygen evolution reaction (OER) and hydrogen evolution reaction (HER). The CoZnCr@MXene catalyst exhibits excellent stability and selective oxidation in alkaline seawater, with MXene incorporation effectively suppressing chloride-induced corrosion while enhancing charge transfer efficiency. Furthermore, when employed in an anion exchange membrane (AEM) electrolyzer, the CoZnCr@MXene catalyst delivers a current density of 500 mA cm^{-2} at an operating voltage of 1.72 V at 60 °C, corresponding to a cell efficiency of 77.8%. The calculated hydrogen production cost is $0.86 per gallon of gasoline-equivalent (GGE), significantly below the 2026 technical target of $2.00/GGE set by the U.S. Department of Energy. This work represents a significant breakthrough in the design of long-lasting, noble-metal-free electrodes for industrial-scale alkaline seawater electrolysis.

Received 4th June 2025
Accepted 21st July 2025

DOI: 10.1039/d5ta04517g

rsc.li/materials-a

Introduction

As a sustainable energy source, hydrogen has the potential to reduce greenhouse gas emissions from conventional fossil fuels and their negative effects on the environment. Water electrolysis is the most appropriate approach to generate high-purity hydrogen as it can efficiently utilize solar and wind energy.[1,2] So far, high-purity water remains the primary raw material for commercial electrocatalytic hydrogen generation. However, the global shortage of freshwater resources (approximately 3% of Earth's water) demands the development of catalytic electrodes based on abundant metal elements for the electrolysis of non-drinkable water sources.[3] Seawater splitting is a prominent alternative as it makes up about 96.5% of the world's total water.[4] One of the main advantages is that seawater, which covers than 70% of the Earth's surface, is readily available and offers an almost infinite supply of feedstock for electrolysis, allaying worries about freshwater shortages. It offers many benefits, such as the ability to produce green hydrogen, reduced competition with fresh water, and the utilization of a plentiful and renewable resource. With the added advantages of affordability, environmental sustainability, and scalability, seawater electrolysis offers a promising way to meet the world's energy needs and help us move toward a sustainable, hydrogen-powered future.[5]

However, dissolved ions in seawater, particularly chloride ions, block the catalytically active sites and reduce the durability and efficiency of seawater splitting.[6] The long-term stability and cost-effectiveness of seawater electrolysis systems are

[a]Department of Inorganic Chemistry, University of Chemistry and Technology Prague, Technická 5, Prague 6, 16628, Praha, Czech Republic. E-mail: soferz@vscht.cz; chauhana@vscht.cz

[b]Institute of Ion Beam Physics and Materials Research, Helmholtz-Zentrum Dresden-Rossendorf, 01328 Dresden, Germany

[c]Institute of Organic Chemistry and Biochemistry, Czech Academy of Sciences, Flemingovo nám. 2, 166 10 Prague 6, Czech Republic

[d]Departament de Química Física i Inorgànica, Universitat Rovira i Virgili, C/ Marcel·lí Domingo, 1, 43007, Tarragona, Spain

[e]Institute of Chemical Research of Catalonia (ICIQ-CERCA), The Barcelona Institut of Science and Technology (BIST), Avinguda Països Catalans 16, Tarragona, 43007, Spain

[f]ICREA, Passeig Lluís Companys, 23, Barcelona, 08010, Spain

† Electronic supplementary information (ESI) available. See DOI: https://doi.org/10.1039/d5ta04517g

significantly hampered by corrosion, particularly when subjected to a harsh, salty environment for long periods. Although various current studies have focused on freshwater electrolysis, alkaline saltwater electrolysis is becoming more and more acknowledged as a practical and beneficial substitute, particularly considering the large and plentiful supply of seawater.[7] Alkaline seawater electrolysis has emerged as a preferred method for seawater splitting, as it eliminates the need for a continuous alkali supply and effectively mitigates the anodic chloride oxidation reaction (COR).[8,9] Recently, many researchers have focused on an anion exchange membrane (AEM) as the separator for seawater electrolysis. However, chloride ions (Cl^-) still appear to pass through the membrane towards the anode under the applied electric field. This results in the unwanted chloride oxidation reaction (ClOR) at the anode, which can cause degradation of the membrane. Therefore, it is essential to develop OER catalysts that have excellent salt tolerance to enhance the advancement of large-scale seawater electrolysis.

Lately, significant reports have been published on low-cost transition metal catalysts such as NiS,[10] MoS_2,[11] and P–$CoNiO_2$,[12] for water splitting in an alkaline medium. Most of the catalysts are not suitable for industrial conditions due to the harsh conditions (60–80 °C, 400 mA cm^{-2}), bubble desorption and low occupancy of hydrogen bubbles at the active sites on the surface of the electrocatalyst due to inappropriate Gibbs free energy.[13] To withstand extreme working conditions, industrial electrocatalysts must fulfil specific requirements such as low-cost materials with fast synthesis routes, active catalyst sites, suitable Gibbs free energy and excellent chemical and structural stability.[14–16] Layered double hydroxides (LDHs) are the most promising candidates to match the above criteria as they exhibit high OER electrocatalysis.[17] The unique structural design exposes the catalyst's active sites and enhances the electrochemical surface area of the OER electrocatalyst.[18] For example, Fe, Co, Ni, Zn, and Mn-based LDHs have been studied widely for the OER.[19–21] Y. Gong *et al.* reported FeCo LDH as a seawater electrocatalyst using a surface corrosion method, achieving an overpotential of 229 mV at a current density of 100 mA cm^{-2}.[22] Y. Park *et al.* concluded that a NiFeCo LDH-based AEM alkaline seawater electrolyzer with a potential of less than 1.72 V can completely suppress the chloride evolution reaction (ClER) thermodynamically.[23] Therefore, developing efficient and durable electrocatalysts that allow for direct seawater electrolysis at low voltage is very desirable.

In this study, we present a highly efficient and stable CoZnCr@Mo_2TiC_2 alkaline seawater electrocatalyst. The electrocatalyst has high durability with a stable long-term performance in alkaline media with a low overpotential of 45 mV at 10 mA cm^{-2} for the HER, which is lower than that of the Pt/C catalyst (58 mV). Similarly, the catalyst provided a low overpotential of 20 mV at 10 mA cm^{-2} for the OER, surpassing that of RuO_2 (49 mV). It required a cell voltage of 1.54 V and 1.62 V to reach current densities of 100 mA cm^{-2} and 200 mA cm^{-2} in an alkaline medium. In addition, the AEM alkaline seawater cell needs a cell voltage of 1.73 V to reach a current density of 0.6 A cm^{-2}, outperforming the state-of-the-art electrolyzer for seawater electrocatalysis. An AEM electrolyzer catalyzed by the CoZnCr@Mo_2TiC_2 electrocatalyst is stable for over 17 days with a faradaic efficiency of 100%. The price of hydrogen (H_2) produced per gallon of gasoline-equivalent (GGE) is $0.89, which is below the U.S. Department of Energy's (DOE) target of $2.00 per GGE by 2026, suggesting superior application prospects. This work provides an optimal approach towards developing a highly efficient, corrosion-resistant and stable industrial-scale catalyst at low potential for seawater electrocatalysis. It delivers a deeper understanding of the factors driving performance enhancement and offers valuable insights for the design of future catalysts.

Methods

Chemicals

Cobalt nitrate hexahydrate ($Co(NO_3)_2 \cdot 6H_2O$), zinc nitrate hexahydrate ($Zn(NO_3)_2 \cdot 6H_2O$), chromium nitrate hexahydrate ($Cr(NO_3)_3 \cdot 9H_2O$), 2-methylimidazole ($C_4H_6N_2$, 2-MIM), ruthenium(IV) oxide (RuO_2) and urea (NH_2CONH_2) were supplied by Lachema. Mo_2TiAlC_2, potassium hydroxide (KOH, Sigma Sigma-Aldrich, 99.99%), Pt/C (20 wt% Pt), sodium chloride (NaCl), Nafion (5 wt% Nafion polymer is dissolved in a combination of lower aliphatic alcohols and water), methanol (CH_3OH), ethanol (C_2H_5OH) and hydrochloric acid (HCl) were purchased from Fluorochem. Nickel foam was obtained from Sigma-Aldrich.

Preparation of ZIF-67

$Co(NO_3)_2$ (894 mg) was dissolved in methanol (5 mL) and stirred for 10 min. 2-MIM (985 mg) was dissolved in methanol (30 mL) and stirred at room temperature for 10 min. Then, both solutions were mixed and stirred at room temperature for 24 h. The product was collected by centrifugation, followed by repeated washings with ethanol and dried at 60 °C overnight.

Preparation of CoZnCr LDH

The CoZnCr LDH was prepared using a hydrothermal method. Briefly, $Zn(NO_3)_2 \cdot 6H_2O$ (150 mg), $Cr(NO_3)_3 \cdot 9H_2O$ (50 mg) and urea (9 mg) were dissolved in ethanol (60 mL) and stirred for 5 min. ZIF-67 powder (50 mg) was added to the solution and stirred for 20 min. The mixture was transferred into a Teflon liner loaded in an autoclave and heated to 120 °C for 6 h. After cooling down to room temperature, the product was isolated by centrifugation using water and ethanol as the dispersing media and dried at 60 °C overnight.

Preparation of LDH@Mo_2TiC_2 MXene

For the preparation of LDH@Mo_2TiC_2, CoZnCr LDH (12 mg) was added to deionized water (10 mL) and stirred for 10 min. In another beaker, Mo_2TiC_2 MXene (1 mg) was added to deionized water (10 mL) and stirred for 10 min. Then, both solutions were mixed together and stirred for 20 min. The solution was then centrifuged at 1000 rpm for 15 min. The product was collected and dried at 60 °C overnight.

Material characterization

The structural and chemical analyses were performed by powder X-ray diffraction (XRD) (Bruker D8, Cu X-ray source, $\lambda = 0.15418$ nm) and X-ray photoelectron spectroscopy (XPS) (SPECS spectrometer equipped with a monochromatic Al Kα X-ray source (1486.7 eV) and a hemispherical electron analyzer Phoibos 150). The morphology and composition of synthesized materials were examined using SEM/STEM (Tescan MAIA 3, Czech Republic) and HRTEM (JEOL 2200 FS, Japan). Detailed structural characterization was carried out using a transmission electron microscope (TEM) (JEOL 2200 FS (Japan)). The bubble contact angles were analyzed *via* ADVEX Instruments, Czech Republic.

Electrochemical measurements

Electrochemical measurements were performed using a potentiostat (Metrohm) with a three-electrode electrochemical system in a laboratory at room temperature. For the preparation of the working electrode, the catalyst powder (LDH@MXene, 3 mg) was mixed with Nafion solution (40 μL) and an ethanol–water mixture (200 μL/100 μL), followed by sonication for 20 min to make an ink like solution, which was then drop-cast on nickel foam (1 × 1 cm active area) and dried at ∼60 °C. For the preparation of Pt/C (40% Pt/C) and RuO_2 (3 mg RuO_2), the same procedure was followed. The as-prepared electrode, Hg/HgO (1 M KOH) and a graphite rod were used as the working, reference and counter electrode for HER analysis, respectively. For the OER measurements, platinum was used as a counter electrode. All potentials were converted to the reversible hydrogen electrode (RHE) using the Nernst equation ($E_{RHE} = E_{Hg/HgO} + 0.0591 + 0.098 \times pH$).[24] Before analysis, the sample was scanned with 20 cycles of cyclic voltammetry (CV) to reach stabilization. Linear sweep voltammetry (LSV) for the HER and OER was recorded with a sweep rate of 10 mV s^{-1} in various electrolyte solutions (1 M KOH, 1 M KOH + NaCl (0 M to sat. NaCl), 1 M KOH + seawater, and natural seawater). For comparison, linear sweep voltammetry of 40% Pt/C (for the HER) and RuO_2 (For the OER) was conducted in 1 M KOH. The Tafel slope was calculated by LSV using the Tafel equation $\eta = b \quad \log(j/j_0)$,[25] where, η is the overpotential, b is the Tafel slope, j is the current density, and j_0 is the exchange current density. Electrochemical impedance spectroscopy (EIS) was conducted in the frequency range from 0.1 Hz and 100 kHz with an amplitude of 10 mV. The durability was measured at a constant current density of 100 mA cm^{-2} for 150 hours in a three-electrode set up. The double-layer capacitance (C_{dl}) of the electrode was evaluated using cyclic voltammetry at different scan rates ranging from 10 mV s^{-1} to 100 mV s^{-1}. The sample names free-standing LDH and supported LDH indicate CoZnCr and CoZnCr@Mo_2TiC_2, respectively.

AEM electrolyzer fabrication

The AEM electrolyzer was assembled using an anode (2.2 cm^2), a cathode (2.2 cm^2), and an anion exchange membrane. Both the anode and cathode were fabricated on nickel foam (2.2 × 2.2 cm^{-2}) by directly depositing the CoZnCr@Mo_2TiC_2 catalyst at a loading of 4 mg cm^{-2}, forming a CoZnCr@Mo_2TiC_2‖□ CoZnCr@Mo_2TiC_2 AEM electrolyzer. For comparison, a RuO_2‖Pt/C electrolyzer was prepared by depositing RuO_2 (4 mg cm^{-2}) onto nickel foam as the anode, while the cathode was prepared by applying Pt/C with Nafion onto nickel foam using the same method as that for the anode. The electrochemical performance of the AEM electrolyzer was evaluated using 1 M KOH and a 1 M KOH + seawater electrolyte, which was introduced into the AEM cell *via* a peristaltic pump at both room temperature and 60 °C. Linear sweep voltammetry (LSV) was performed at a scan rate of 10 mV s^{-1}. The long-term stability of the electrolyzer was measured *via* chronopotentiometry at a constant current density of 500 mA cm^{-2} over 410 h. The internal cell temperature was maintained at 60 °C by continuously circulating a preheated electrolyte (60 °C) through the system. Faradaic efficiency (FE) was determined using the drainage method at a constant current density of 500 mA cm^{-2} in 1 M KOH + seawater.

Results and discussion

Preparation and characterization of the CoZnCr LDH@Mo_2TiC_2 MXene

We used the self-assembly method to synthesize CoZnCr@Mo_2TiC_2, as presented in Fig. 1 (see Methods for details). Scanning electron microscopy revealed a well-defined dodecahedral morphology (Fig. 2a).[26] Upon transformation of ZIF-67 into CoZnCr LDH, the initially smooth surface evolved into a nanosheet-clustered structure, as shown in Fig. 2b.[27] The incorporation of Mo_2TiC_2 MXene into CoZnCr-LDH preserved the nanosphere-like architecture of LDH while introducing nanoparticle-wrapped surfaces (Fig. 2c).

To further investigate the structural and compositional characteristics, scanning transmission electron microscopy (STEM) was employed, confirming the retention of the dodecahedral shape in CoZnCr@Mo_2TiC_2, as shown in Fig. 2d. Elemental mapping of Co, Zn, Cr, Mo, Ti, and C demonstrated a uniform distribution of elements throughout the composite (Fig. 2e). High-resolution transmission electron microscopy (HRTEM) revealed the presence of a distinct hollow nanocage structure, shown in Fig. 2f and g, in agreement with the SEM observations. The presence of hollow cavities within CoZnCr@Mo_2TiC_2 serves as an electrolyte reservoir, enhancing the contact between electrolyte ions and the material, thereby facilitating electrochemical reactions.[28] The selected area electron diffraction (SAED) pattern (inset, Fig. 2g) further confirms the crystallinity of the synthesized composite. Fig. 2h and i depict well-resolved lattice fringes with an interplanar spacing of 0.25 nm and 1.12 nm, corresponding to the (012) and (002) planes of LDH and MXenes, respectively, which XRD[29] further confirmed. The XRD pattern of CoZnCr@Mo_2TiC_2 aligns with the characteristic peaks of both Mo_2TiC_2 and CoZnCr, as presented in ESI Fig. 1a and b†. Notably, the diffraction peaks at 31.7° and 36.2° correspond to the (012) and (015) planes of CoZnCr, while the peak at 7.3° is indexed to the (002) plane of Mo_2TiC_2, consistent with the HRTEM results. The chemical state of CoZnCr@Mo_2TiC_2 was investigated using X-ray

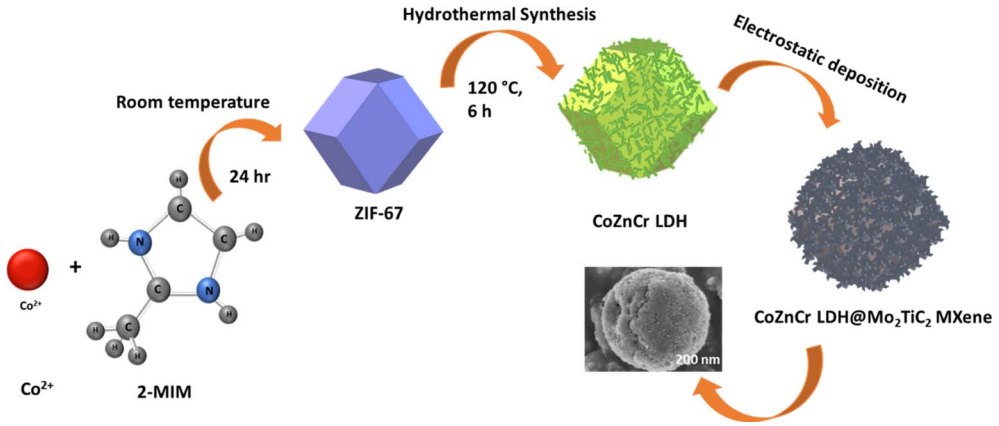

Fig. 1 Schematic illustration of the synthesis process of CoZnCr@MXene.

photoelectron spectroscopy (XPS). The Zn 2p spectrum exhibits two distinct peaks at 1023.6 eV and 1046.6 eV, corresponding to Zn $2p_{3/2}$ and Zn $2p_{1/2}$, respectively, indicating the presence of Zn^{2+} (ESI Fig. 2a†).

Similarly, the Cr 2p XPS spectrum of the composite (ESI Fig. 2b†) shows two distinct peaks at 579.4 eV and 589.1 eV, corresponding to Cr $2p_{3/2}$ and Cr $2p_{1/2}$, respectively. These binding energies are characteristic of chromium in the +3 oxidation state (Cr(III)), indicating that chromium is predominantly present as Cr(III) species in the material. This confirms the oxidation state of chromium and supports the understanding of its chemical environment within the composite structure. The deconvolution of the high-resolution spectrum of the Mo 3d region suggests the presence of Mo in two oxidation states, Mo^{4+} and Mo^{6+}, respectively. The peaks at 231.0 and 234.2 eV correspond to the $3d_{5/2}$ and $3d_{3/2}$ components of Mo^{4+}, respectively, and peaks at 234.7 and 237.7 eV correspond to the same components of Mo^{6+} as shown in ESI

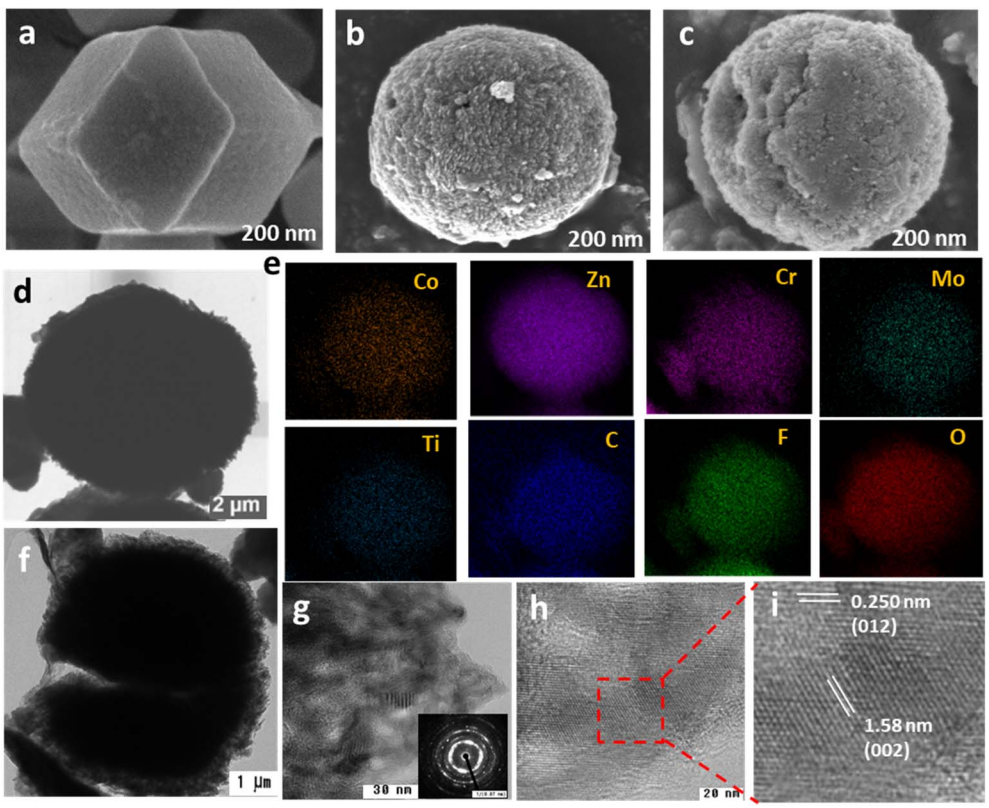

Fig. 2 SEM image of as-prepared (a) ZIF-67, (b) CoZnCr and (c) CoZnCr@Mo_2TiC_2. (d) STEM image of as prepared CoZnCr@Mo_2TiC_2. (e) Elemental mapping showing the uniform distribution of Co, Zn, Cr, Mo, Tl and C. (f and g) HRTEM image of CoZnCr@Mo_2TiC_2. (h and i) Lattice fringes of CoZnCr and Mo_2TiC_2.

Fig. 2c.†[29,30] The XPS C 1s spectrum reveals peaks at 286.9 eV, 285.7 eV, and 282.2 eV, which are assigned to C–O, C–C, and Mo(Ti)–C bonds, respectively (ESI Fig. 2d†). Additionally, the O 1s spectrum displays peaks at 532.4 eV and 534.0 eV, corresponding to Mo–OH and O–C species, respectively, as shown in ESI Fig. 2e.†

Electrocatalysts for alkaline electrolysis

Half-cell performance of the CoZnCr@Mo_2TiC_2 electrode. The electrochemical performance of the CoZnCr@Mo_2TiC_2 electrode was evaluated using half-cell water electrolysis in a 1.0 M KOH electrolyte. To assess the HER activity, linear sweep voltammetry (LSV) measurements were performed for various catalysts. CoZnCr@Mo_2TiC_2 demonstrated superior HER performance, exhibiting a low overpotential of 45 mV at 10 mA cm^{-2} and 141 mV at 100 mA cm^{-2}, outperforming ZIF-67 (297 mV at 100 mA cm^{-2}), CoZnCr (208 mV at 100 mA cm^{-2}), and commercial Pt/C (214 mV at 100 mA cm^{-2}), as shown in Fig. 3a. In contrast, the Tafel plots (Fig. 3b) reveal that Pt/C has a lower overpotential at a given current density, reflecting faster intrinsic reaction kinetics. This difference highlights that while Pt/C excels in catalytic kinetics at low overpotentials, CoZnCr@MXene outperforms Pt/C in delivering higher current densities due to enhanced active site availability and electron transport. Additionally, the CoZnCr@Mo_2TiC_2 electrode exhibited a Tafel slope of 90 mV dec^{-1}, which suggests that the rate-determining step is the Heyrovsky pathway. Additionally, the obtained value is lower than that of Pt/C (112 mV dec^{-1}), indicating enhanced HER kinetics and superior catalytic efficiency compared to those of the commercial 40% Pt/C catalyst. Furthermore, CoZnCr@Mo_2TiC_2 achieved significantly higher current densities of 500 mA cm^{-2} and 1000 mA cm^{-2}, surpassing that of commercial Pt/C, which highlights its potential for industrial applications (ESI Fig. 3a†). Electrochemical impedance spectroscopy (EIS) analysis of CoZnCr@Mo_2TiC_2 demonstrates its efficient charge transfer, as

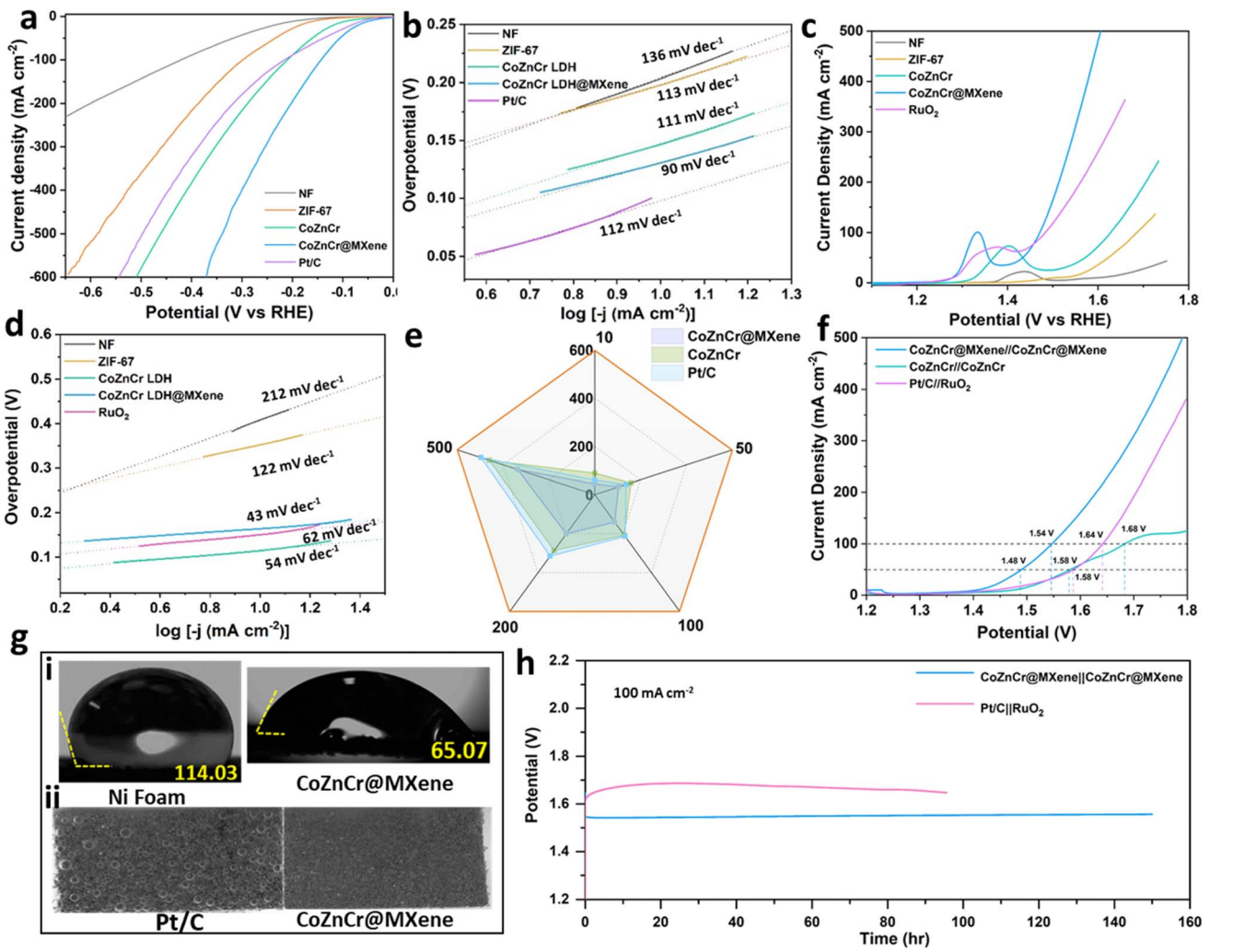

Fig. 3 Electrochemical performance. (a) HER polarization curves of CoZnCr@MXene, CoZnCr, ZIF-67, Pt/c and Ni foam in 1 M KOH. (b) Tafel slopes of the five electrocatalysts. (c) OER polarization curves of CoZnCr@MXene, CoZnCr, ZIF-67, RuO_2 and Ni foam in 1 M KOH. (d) Tafel slopes of the five electrocatalysts. (e) Comparative overpotential of the three different electroctalysts at various current densities. (f) Polarization curves of overall water splitting (OWS) in 1 M KOH. (g) (i) Contact angles (static water droplet) for CoZnCr@MXene and Ni foam. (ii) Digital photos demonstrate the hydrogen release behavior. (h) Long-term stability test at 100 mA cm^{-2}.

indicated by its low charge transfer resistance (R_{ct}) of 4.17 Ω, which is lower than that of commercial Pt/C (5.53 Ω), as shown in ESI Fig. 3b† (inset: equivalent circuit diagram). The electrochemical surface area (ECSA) of the catalyst was determined by measuring the double-layer capacitance (C_{dl}) from cyclic voltammetry (CV) scans at different scan rates. CoZnCr@Mo_2TiC_2 exhibits a significantly higher C_{dl} of 22 mF compared to CoZnCr (11 mF), indicating a larger ECSA and a greater number of electrochemically active sites (ESI Fig. 4a–d†). Beyond the HER, the oxygen evolution reaction (OER) plays a crucial role in water electrolysis. The OER catalytic performance of different electrodes was evaluated under identical conditions to those of the HER. As shown in Fig. 3c and d, the CoZnCr@Mo_2TiC_2 electrode exhibits outstanding OER activity, requiring a low overpotential of 20 mV to achieve a current density of 10 mA cm^{-2}, with a Tafel slope of 47 mV dec^{-1}.

These values are significantly lower than those of RuO_2 (49 mV), highlighting the superior OER kinetics of CoZnCr@Mo_2TiC_2. Additionally, to reach a current density of 50 mA cm^{-2} CoZnCr@Mo_2TiC_2 required an overpotential of 180 mV. For comparison, the overpotential and Tafel slope values of recently reported OER electrocatalysts are summarized in ESI Table S1.† Fig. 3e presents the overpotential required at various current densities for different catalysts, highlighting the superior HER activity of CoZnCr@Mo_2TiC_2 across the entire current density range. Notably, at a high current density of 500 mA cm^{-2}, CoZnCr@Mo_2TiC_2 requires an overpotential of only 339 mV, which is significantly lower than that of the commercial 40% Pt/C catalyst (497 mV). This remarkable performance underscores the exceptional catalytic efficiency and robust stability of CoZnCr@Mo_2TiC_2, particularly at high current densities, making it a promising candidate for practical electrocatalytic applications. Furthermore, to investigate the OER pathway, pH-dependent measurements were performed in KOH solutions (pH 13.0–14.0). The overpotential increased with decreasing pH, indicating proton-coupled electron transfer consistent with the Adsorbate Evolution Mechanism (AEM). This trend rules out the Lattice Oxygen Mechanism (LOM), which typically shows weak or irregular pH dependence. (ESI Fig. 5†). The CoZnCr@Mo_2TiC_2‖CoZnCr@Mo_2TiC_2 electrode exhibits outstanding overall water-splitting performance, requiring a remarkably low cell voltage of 1.48 V at 50 mA cm^{-2} and 1.40 V at 10 mA cm^{-2}. This performance surpasses that of the commercial Pt/C‖RuO_2 electrode (1.58 V) and represents one of the best values reported to date (ESI Fig. 6 and Table S2†), as illustrated in Fig. 3f. The wettability of the electrode surface plays a crucial role in catalytic performance, particularly at high current densities, as it influences mass transport and electrolyte penetration. To assess this, the contact angle (CA) of a water droplet on the electrode surface was measured. As shown in Fig. 3g (i), the CoZnCr@Mo_2TiC_2 electrode exhibits a significantly smaller contact angle of 65°, indicating superior wettability compared to Ni foam (114°). Enhanced wettability improves the electrode–electrolyte interface, facilitating better electrolyte infiltration and mass transport.[31,32] Furthermore, hydrogen bubble release observations reveal that large bubbles formed on Pt/C electrodes in comparison to CoZnCr@Mo_2TiC_2 (Fig. 3g(ii)), which indicates variations in gas release behavior. Larger bubbles on Pt/C suggest delayed detachment, potentially due to surface wettability or bubble adhesion forces. In contrast, smaller bubbles on CoZnCr@Mo_2TiC_2 imply more efficient bubble detachment and dispersion, which can enhance reactant diffusion to the catalytic surface. However, these differences do not affect intrinsic reaction kinetics, which is governed by thermodynamics and catalyst conductivity. The long-term operational stability of CoZnCr@Mo_2TiC_2 for overall water splitting (OWS) was evaluated in a two-electrode system under alkaline conditions (1 M KOH). As shown in Fig. 3h, the cell voltage remains nearly unchanged over 150 hours of continuous operation, demonstrating remarkable durability and stability at high current densities. The stable performance of CoZnCr@MXene reflects the robustness of its engineered interface and composition. Strong coupling between the LDH active phase and the conductive MXene support ensures reliable electrical contact and prevents agglomeration or detachment of active sites. This finding is consistent with recent reports demonstrating that interface engineering in LDH–MXene composites enhances electrocatalytic durability. In contrast, the commercial Pt/C‖RuO_2 catalyst exhibits an initial increase in potential followed by a gradual decline during the same period. This behavior is likely due to surface activation of RuO_2 at the beginning of electrolysis, followed by progressive degradation. Ru-based catalysts are known to undergo oxidative dissolution and structural changes under prolonged alkaline conditions, leading to a loss of active sites and reduced stability over time.[33,34] This outstanding long-term performance highlights the robustness of CoZnCr@Mo_2TiC_2 as a promising electrocatalyst for practical water-splitting applications.

Salinity test of the catalyst. The electrocatalytic activity of the CoZnCr@Mo_2TiC_2 electrocatalyst was systematically investigated in an alkaline electrolyte with varying NaCl concentrations (ranging from 0 M to saturation). Remarkably, the catalyst maintains excellent HER and OER kinetics even in a saturated NaCl solution, as illustrated in Fig. 4a and b. For the HER, the overpotential exhibits a slight increase of 53 mV when transitioning from 0 M to saturated NaCl, indicating stable catalytic efficiency under saline conditions. Similarly, for the OER, the overpotential increases from 68 mV (0 M NaCl) to 131 mV (saturated NaCl), demonstrating a moderate variation of 63 mV (Fig. 4c), at a current density of 10 mA cm^{-2}. These results demonstrate the catalyst's remarkable salt tolerance and electrochemical stability. Notably, its catalytic performance is stable with increasing salt concentration, consistent with the experimental observations, underscoring the potential of CoZnCr@Mo_2TiC_2 for electrocatalytic applications in saline and seawater environments.

The cycliing stability of the CoZnCr@Mo_2TiC_2 catalyst was evaluated by comparing the linear sweep voltammetry (LSV) curves for the HER and OER before and after 10 000 cycles in a 1 M NaCl + 1 M KOH electrolyte. As shown in Fig. 4d, the CoZnCr@Mo_2TiC_2 catalyst demonstrates stable catalytic performance, with only a 19 mV increase in overpotential for the HER and a negligible 6 mV increase for the OER (Fig. 4d inset) at a current density of 10 mA cm^{-2}. Furthermore, the long-term

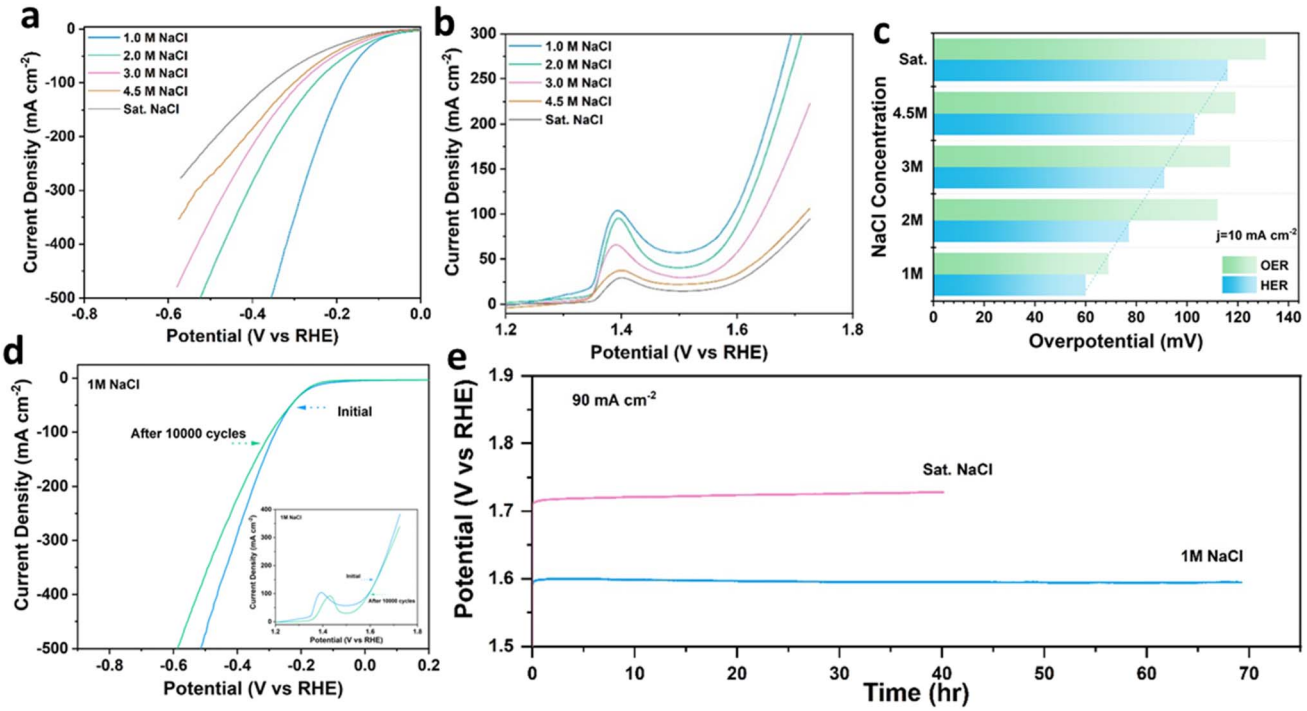

Fig. 4 (a) LSV curves of CoZnCr@MXene for the HER in different salt solutions. (b) LSV curves of CoZnCr@MXene for the OER in different salt solutions. (c) Corresponding histogram of the overpotential (HER and OER) at 10 mA cm^{-2}. (d) Polarization curves of CoZnCr@MXene before and after 10 000 cycles for the HER; inset: LSV curves for the OER before and after 10 000 cycles. (e) Chronopotentiometry curves for the OER in 1.0 M KOH with 1 M NaCl and sat. NaCl at 90 mA cm^{-2}.

stability of the CoZnCr@Mo_2TiC_2 catalyst was assessed using a chronopotentiometric (CP) test at a current density of 90 mA cm^{-2} at various salt concentrations. In the 1 M NaCl electrolyte, no significant loss in current density was observed over 70 hours of continuous operation, highlighting the catalyst's excellent resistance to salinity. Notably, the catalyst maintained outstanding durability without any noticeable degradation, even in a saturated NaCl electrolyte over a 40 hour test, further demonstrating its superior durability (Fig. 4e). These findings highlight the CoZnCr@Mo_2TiC_2 electrocatalyst as a promising candidate for seawater splitting applications, owing to its high corrosion resistance, excellent salt tolerance, and long-term stability.

Electrocatalytic seawater performance of the catalysts. Seawater electrolysis presents a cost-effective and abundant alternative to freshwater electrolysis; however, its suitability as an electrolyte for efficient electrolyzer operation must be carefully evaluated.[35] In this study, the electrocatalytic activity of CoZnCr@Mo_2TiC_2 for overall water splitting was assessed in both 1 M KOH + seawater and natural seawater. The catalyst required cell potentials of 1.55 V and 1.58 V to achieve a current density of 50 mA cm^{-2} in 1 M KOH + seawater and natural seawater, respectively, as shown in Fig. 5a. Notably, the cell potential required in natural seawater (1.58 V at 50 mA cm^{-2}) is significantly lower than that of the Pt/C||RuO_2 electrode (1.69 V at 50 mA cm^{-2}), as seen in ESI Fig. 7a.† The CoZnCr@MXene catalyst exhibited overpotentials of 73 mV (HER) and 71 mV (OER) in 1 M KOH + seawater, and 86 mV (HER) and 129 mV (OER) in natural seawater (10 mA cm^{-2}), demonstrating superior HER and OER kinetics compared to other catalysts, as shown in ESI Fig. 7b and c.† At higher potentials, the LSV curves in 1 M KOH + seawater (Fig. 5c) exhibit a deviation from the linear trend observed in 1 M KOH (Fig. 5b), indicating possible mass transfer limitations. This behavior can be attributed to the complex ionic composition of seawater, which contains additional ions such as Cl^-, SO_4^{2-}, Mg^{2+}, and Ca^{2+}. These species can interfere with hydroxide ion transport, alter electrolyte conductivity, and contribute to the formation of surface-adsorbed layers or precipitates on the catalyst surface, thereby impeding access to active sites. In contrast, the simpler and more conductive 1 M KOH electrolyte supports more efficient mass transport, resulting in a continuous increase in current density with potential. This highlights the influence of electrolyte composition on catalytic performance, especially under high current conditions.

These results demonstrate the potential of CoZnCr@Mo_2TiC_2 as a promising electrocatalyst for seawater electrolysis, with excellent performance in both the HER and OER under practical, seawater-based conditions. The typical operating temperature for industrial water electrolysis systems ranges between 50 and 90 °C to reduce the total voltage required for water splitting.[36] To bridge the gap between laboratory conditions and commercial applications, the electrochemical performance of CoZnCr@MXene was evaluated at these temperatures in a three-electrode system. As the temperature of the alkaline and alkaline seawater electrolytes increased from

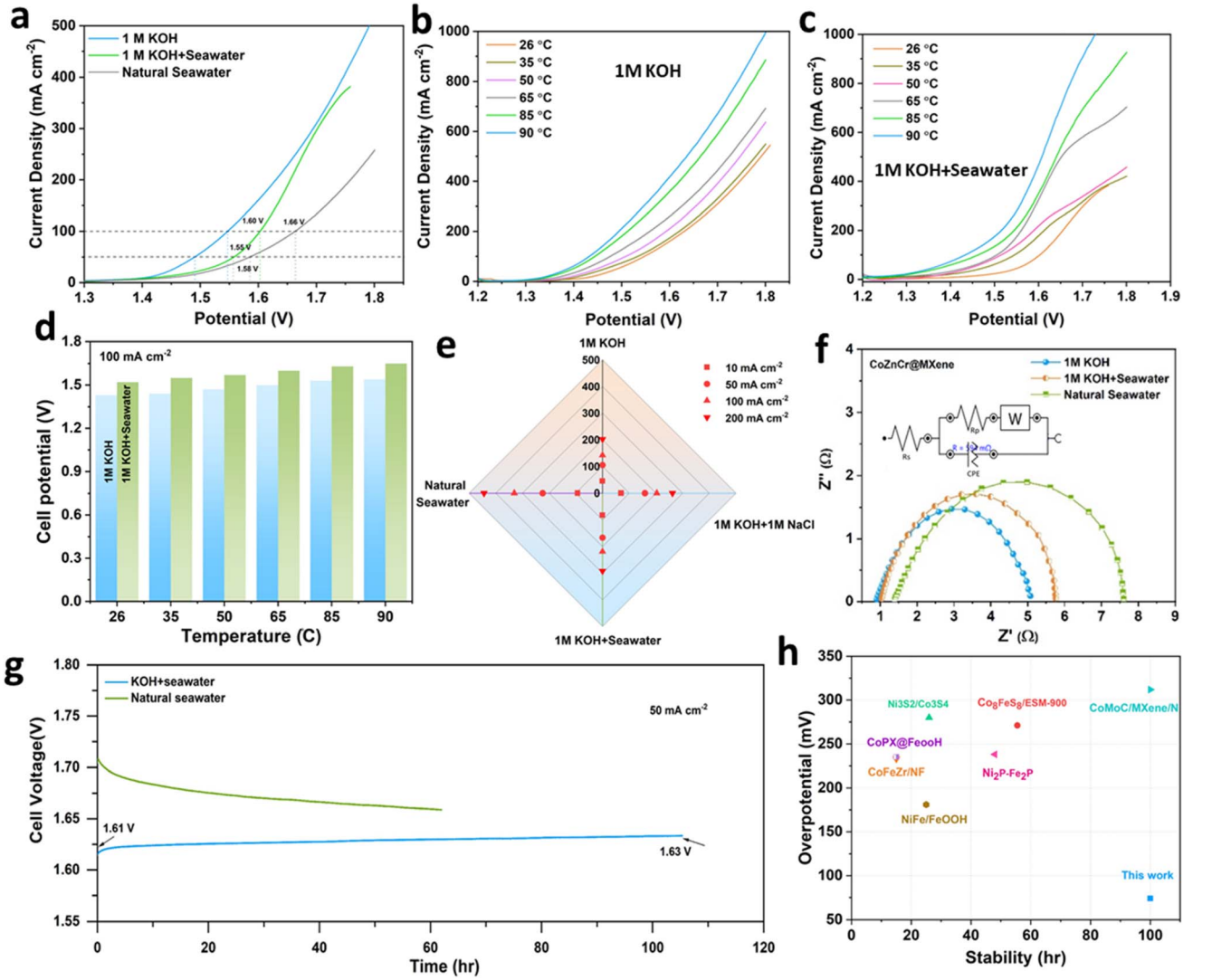

Fig. 5 Catalytic performance in different electrolytes: (a) LSV curves of the CoZnCr@MXene‖ CoZnCr@MXene catalyst in various electrolytes at 26 °C. The polarization curves of CoZnCr@MXene‖ CoZnCr@MXene for overall water splitting at different temperatures, (b) in 1 M KOH and (c) in 1 M KOH + seawater. (d) A cell potential of CoZnCr@MXene‖ CoZnCr@MXene to reach 100 mA cm^{-2} current density in 1 M KOH and 1 M KOH + seawater electrolyte. (e) The HER overpotentials of the CoZnCr@MXene electrocatalyst to achieve current densities of 10–200 mA cm^{-2} in various electrolytes. (f) EIS curves. (g) Chronopotentiometric curve at 50 mA cm^{-2} in 1 M KOH + seawater and natural seawater. (h) Overpotential and long-term stability compared with those in the literature. The Tafel slopes and long-term stability data are from references (ESI Table S5†).

26 °C to 90 °C, the voltage required for water splitting decreased, as shown in Fig. 5b and c. At elevated temperatures, CoZnCr@MXene achieved a current density of 1000 mA cm^{-2}, outperforming Pt/C‖RuO_2 (ESI Fig. 7d†).

The catalyst facilitated overall water splitting with a cell voltage of 1.52 V at 26 °C in 1 M KOH + seawater at a current density of 100 mA cm^{-2}, as shown in Fig. 5d. When comparing the cell voltage at 100 mA cm^{-2} in 1 M KOH and 1 M KOH + seawater, only an additional 0.09 V (at 26 °C) was required in the seawater electrolyte, highlighting the potential of CoZnCr@MXene for industrial water electrolysis applications. Fig. 5e demonstrates the overpotentials of CoZnCr@MXene to achieve current densities of 10, 50, 100, and 200 mA cm^{-2}, showing only a 10–20 mV change across four different electrolytes at a particular current density (ESI Table 3†), confirming its efficacy in alkaline, saline, and seawater electrolytes. Furthermore, CoZnCr@MXene exhibits a low charge transfer resistance of 4.74 Ω in 1 M KOH + seawater, further emphasizing its rapid reaction kinetics (Fig. 5f and ESI Table 4†). Chronoamperometric measurements demonstrate the excellent durability of the CoZnCr@MXene catalyst with minimal cell voltage decay over 100 hours of continuous operation in 1 M KOH + seawater and 60 hours of continue operation in natural seawater, as shown in Fig. 5g. To better highlight the performance of our catalyst, we compared it with recent state-of-the-art seawater electrolyzers. As shown in Fig. 5h and detailed in ESI Table S5,† our catalyst delivers a low overpotential of 74 mV at 10 mA cm^{-2} and maintains excellent stability over 100 hours. In contrast, a NiFe LDH/FeOOH catalyst shows 181 mV with 25 hour stability, and CoMoC/MXene/N exhibits 312 mV with 100 hours

of stability. These comparisons demonstrate that our catalyst offers a superior combination of activity and durability under harsh alkaline seawater conditions, making it a promising candidate for practical seawater electrolysis applications. Additionally, the decreasing cell voltage for natural seawater indicates improved energy conversion efficiency of water splitting. The CoZnCr@MXene catalyst demonstrates significantly faster reaction kinetics and exceptional stability compared to other reported non-noble metal catalysts (Fig. 5g and ESI Table S5†). Inductively coupled plasma (ICP-OES) analysis of electrolytes shows very low concentrations of Zn, Cr and Mo ions after the long-term stability test, confirming negligible leaching and demonstrating that the material is effectively resistant to corrosion and oxidation (ESI Table S6†). Post-test scanning electron microscopy (SEM) images (ESI Fig. 8a†) show that the CoZnCr@MXene catalyst retains its surface morphology, further confirming its robust structural integrity. The catalyst exhibits outstanding corrosion resistance against chloride ions and other complex ionic species present in seawater, along with superior structural stability at high current densities. X-ray diffraction (XRD) analysis of the post-OER electrodes shows negligible changes in peak positions across various planes, further supporting the chemical stability of CoZnCr@MXene under seawater conditions (ESI Fig. 8b†). Additionally, X-ray photoelectron spectroscopy (XPS) analysis (ESI Fig. 8c†) reveals a positive shift in all peaks, which is indicative of enhanced OER kinetics.[37,38] These findings suggest that the CoZnCr component plays a pivotal role in providing resistance to chloride-induced corrosion,[39,40] contributing to the catalyst's efficient catalytic activity and outstanding stability for alkaline seawater electrolysis.

Mechanism understanding. To gain a deeper understanding of the relationship between the catalyst and its electronic structure, density functional theory (DFT) calculations were performed on model structures of CoZnCr and MXenes. The results reveal a relatively low number of antibonding states in CoZnCr@MXene, which further supports the stability of the computational model (ESI Fig. S9a and b†). The electronic coupling between CoZnCr and Mo_2TiC_2 is shown in ESI Fig. 10a–f.† The results demonstrate that hybridization between CoZnCr and Mo_2TiC_2 leads to charge redistribution, shifting the density of states near the Fermi level and enhancing the catalytic activity of active sites. The total density of states (DOS) analysis shows that CoZnCr@Mo_2TiC_2 has a larger electron density around the Fermi level compared to CoZnCr (Fig. 6a and ESI 11a and b†). The results imply that the thorough restructuring of the catalyst boosts its electrical conductivity, allowing for efficient electron transfer in electrocatalysis.

To determine the most favorable surface-active site for each intermediate step, we compared the adsorption energies across different surface sites. In the case of the HER (Fig. 6b), the Gibbs free energy values of the key intermediates (*H) on

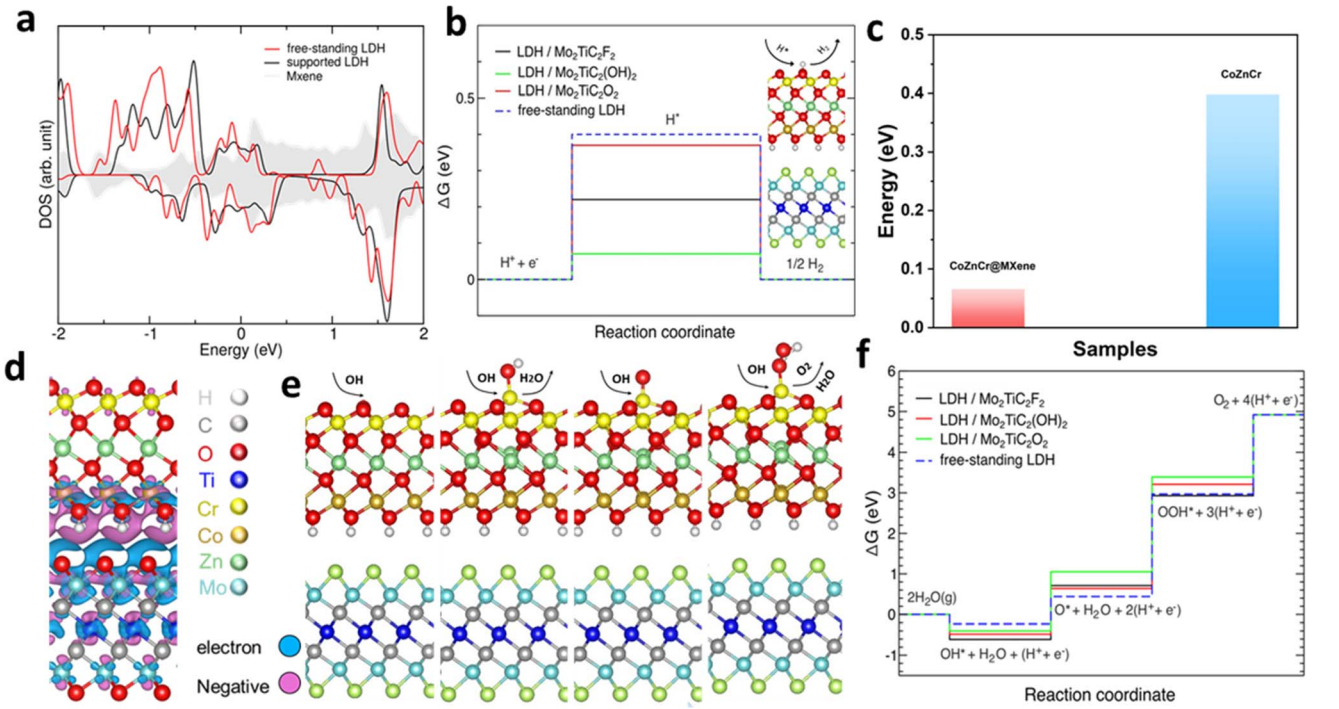

Fig. 6 (a) Projected density of states for CoZnCr on Mo_2TiC_2 with surface terminations of CoZnCrO$_4$H/$Mo_2TiC_2O_2$. (b) Free energy profiles of the HER for free-standing and supported CoZnCr on Mo_2TiC_2 with different surface terminations; optimized atomic structures are shown as inserted images. (Note: the results are obtained at external potential Uext = 0.0 V). (c) Free energy of adsorbed H* intermediates (ΔGH*) on CoZnCr@Mo_2TiC_2 and CoZnCr. (d) Charge transfer between CoZnCr and Mo_2TiC_2 with different surface terminations. The blue and violet isosurfaces show electron and hole accumulations. (e) Optimized atomic structures for the OER. (f) Free energy profiles of the OER for free-standing and supported CoZnCr on Mo_2TiC_2 with different surface terminations (Note: the results are obtained at external potential Uext = 0.0 V).

freestanding LDH are positive, with a minimum barrier of 0.4 eV. It is evident that the presence of MXenes significantly influences the HER energy barrier of the heterostructure compared to the freestanding CoZnCr (see Table S7†). CoZnCr@$Mo_2TiC_2(OH)_2$ exhibits the lowest energy barrier among the different considered surface terminations, suggesting high catalytic activity for the HER. Moreover, the free energy of hydrogen adsorption (ΔGH*) is a key parameter influencing HER performance, with a value close to zero suggesting optimal H adsorption and efficient H_2 release. The calculated ΔGH* value for CoZnCr@ Mo_2TiC_2 is 0.06 eV, which is nearer to the thermoneutral point compared to the values for CoZnCr (0.39 eV) (Fig. 6c), indicating a surface that facilitates the efficient desorption of the evolved hydrogen species. Notably, hybridization is more pronounced in the case of CoZnCr and $Mo_2TiC_2O_2$, resulting in the highest charge transfer and interfacial binding energies, as shown in Fig. 6d and Table S8.† This strong interaction effectively lowers the energy barrier for *OOH formation, the rate-limiting step, further improving OER efficiency. The structural configurations of intermediates (Fig. 6e) reveal that Cr atoms serve as the most favorable adsorption sites for stabilizing intermediates during the OER process. Free energy profile calculations (Fig. 6f) indicate that the rate-limiting step in supported heterostructures corresponds to the transformation of [O*] into [*OOH], consistent with a previous report.[41] However, the overpotential is lower than that of freestanding LDH under similar conditions, suggesting faster OER kinetics on CoZnCr@Mo_2TiC_2. Thus, the incorporation of Mo_2TiC_2 modifies the Gibbs free energy landscape of the HER-OER pathway and tunes the electronic structure of the catalyst, resulting in enhanced HER and OER activity.

Performance of an AEM seawater electrolyzer. We further assembled an alkaline seawater AEM electrolyzer utilizing CoZnCr@MXene as both the anode and cathode, as depicted in Fig. 7a. The polarization curve for overall water splitting in 1 M KOH + seawater reveals that the electrolyzer requires a cell voltage of 1.64 V to achieve a current density of 100 mA cm^{-2} at 26 °C, which is significantly lower than that of the commercial Pt/C||RuO_2 electrolyzer (1.77 V) at the same current density, as shown in Fig. 7b. For further comparison, the performance of Pt–RuO_2//Pt–RuO_2 at 60 °C is also included in Fig. 7b. This demonstrates that the CoZnCr@MXene-based AEM electrolyzer outperforms commercial electrocatalysts in terms of efficiency. Additionally, using a drainage-gas collection method, the O_2 gas production from the CoZnCr@MXene electrolyzer was measured (ESI Fig. 12a and b†), yielding a faradaic efficiency of 99% in an alkaline seawater electrolyte, as shown in Fig. 7c. The catalyst also exhibited exceptional durability, maintaining stable performance at a current density of 200 mA cm^{-2} for 16.8 days, with negligible cell voltage degradation, indicating outstanding stability and high selectivity for alkaline seawater electrolysis, as demonstrated in Fig. 7d. Furthermore, the CoZnCr@MXene||CoZnCr@MXene-catalyzed AEM electrolyzer exhibits a cell efficiency of 77.8%, surpassing the U.S. Department of Energy's (DOE) target efficiency of 77%, at a current density of 0.2 A cm^{-2} (ESI Fig. 12c and ESI Note 1†). Additionally, a critical metric of the electrolyzer's economic viability is the hydrogen production cost, which is calculated to be as low as $0.86 per GGE of H_2, as detailed in ESI Note 1.† This value is

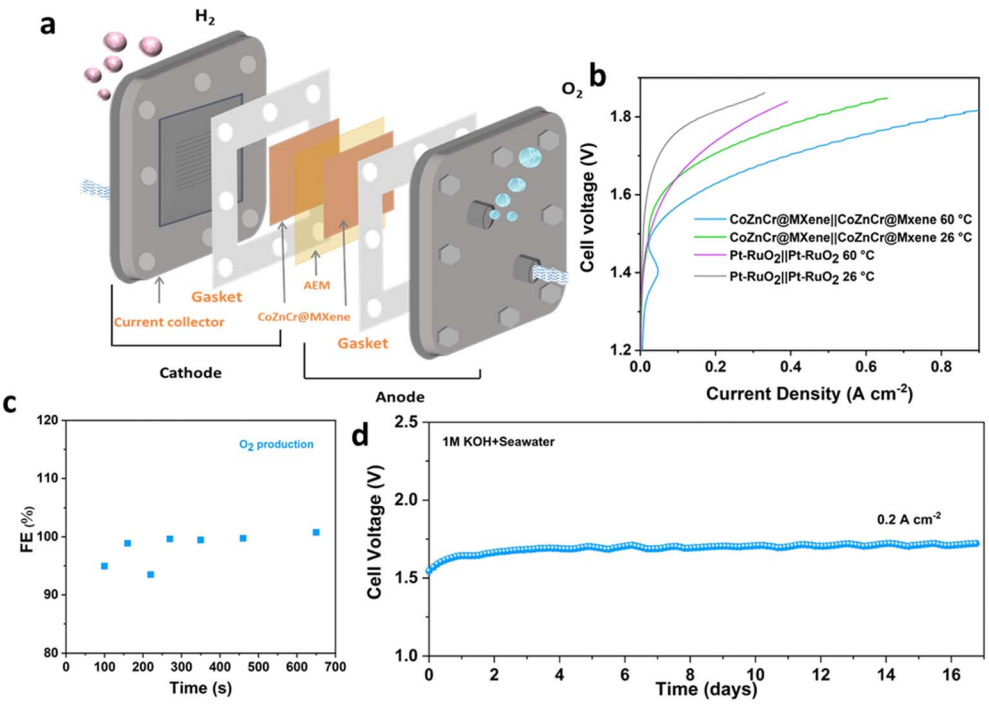

Fig. 7 AEM electrolyzer performance in alkaline seawater. (a) Schematic illustration of the AEM electrolyzer. (b) Polarization curves of CoZnCr@MXene|| CoZnCr@MXene in 1 M KOH + seawater at 26 °C and 60 °C and with Pt/C||RuO_2 at 26 °C and 60 °C. (c) FE of producing O_2. (d) Durability test of the CoZnCr@MXene|| CoZnCr@MXene AEM electrolyzer in 1 M KOH + seawater electrolyte at 200 mA cm^{-2}.

less than half of the DOE's 2026 target of $2.00 per GGE, demonstrating the potential for economical hydrogen production.[42] These results highlight a promising pathway for the efficient and cost-effective production of H_2 and O_2 *via* seawater electrolysis, facilitated by outstanding catalytic activity and stability. This remarkable performance can be attributed to (1) the unique nanocage architecture, which facilitates optimal interface interaction and creates a high density of active catalytic sites; (2) the synergistic interplay between the catalyst's hierarchical structure and compositional attributes, which enhance the interfacial electron transfer between active sites and the substrate, thereby significantly improving the intrinsic catalytic activity; and (3) the chloride ion resistance of CoZnCr@MXene, which minimizes Cl^- interference, promotes the H_2O–OH^- reaction pathway, and ensures selective catalysis.

Conclusion

In summary, we successfully developed a CoZnCr@MXene electrocatalyst for selective, efficient and highly stable alkaline seawater electrolysis at higher current densities. The hierarchical hollow structures enhance the diffusion of reactants and products to and from the catalytic sites. Increasing the number of such sites lowers the overall activation energy and promotes efficient electron transfer, facilitating faster charge transfer and reaction kinetics. The catalyst displays a good HER and OER performance with a low overpotential of 45 mV and 20 mV at 10 mA cm^{-2} in an alkaline medium, respectively. Notably, the catalyst exhibits an impressive performance, with an overpotential increase of less than 63 mV as the salt concentration in the electrolyte increases from 0 M to saturated NaCl. Moreover, CoZnCr@MXene exhibits a low cell voltage of 1.60 V at 100 mA cm^{-2} current density in alkaline seawater electrolyte, demonstrating the higher stability for the electrocatalytic seawater OER. The CoZnCr@MXene AEM seawater electrolyzer achieves high performance with a cell voltage of 1.83 V at 1000 mA cm^{-2} under industrial conditions with a high cell efficiency of 77.8% and durability over 16.8 days (0.2 A cm^{-2}) in alkaline seawater electrolyte. Moreover, the DFT calculations revealed that MXene plays a crucial role in enhancing HER and OER performance by significantly improving electroactivity, strengthening adsorbate binding, and facilitating efficient electron transfer. The result outperforms those of reported articles in seawater electrolysis. The results provide important insights for effective electrolyzer design and a strategic approach to catalyst development for seawater electrolysis with low energy consumption.

Data availability

The datasets generated during and/or analyzed during the study are accessible *via* the Zenodo repository: **https://doi.org/10.5281/zenodo.15100523**.

Conflicts of interest

There are no conflicts to declare.

Acknowledgements

P.C. acknowledges the financial support from the European Union's Horizon Europe research and innovation program under the Marie Skłodowska – Curie grant agreement No. 101130803. AVK acknowledges funding from the German Research Foundation (DFG), project KR 4866/9–1 and the collaborative research center "Chemistry of Synthetic 2D Materials" CRC-1415-417590517. Generous CPU time grants from the Paderborn Center for Parallel Computing (PC2, Noctua 2 cluster, hpc-prf-def2dhet) and Gauss Centre for Supercomputing e.V. (**www.gauss-centre.eu**), Supercomputer HAWK at Höchstleistungsrechenzentrum Stuttgart (**www.hlrs.de**), are greatly appreciated. This work was supported by the project "The Energy Conversion and Storage" funded as project No. CZ.02.01.01/00/22_008/0004617 by Programme Johannes Amos Commenius, call Excellent Research. B. K. acknowledges the grant PID2022-139176OA-I00 funded by MICIU/AEI/ 10.13039/501100011033 and, as appropriate, by "ERDF A way of making Europe" and by the "European Union". Z. S. was supported by Czech Science Foundation (GACR No. 23-05918S).

References

1 X. Han, X. Wu, Y. Deng, J. Liu, J. Lu, C. Zhong and W. Hu, *Adv. Energy Mater.*, 2018, **8**, 1–12.
2 P. Liu, B. Chen, C. Liang, W. Yao, Y. Cui, S. Hu, P. Zou, H. Zhang, H. J. Fan and C. Yang, *Adv. Mater.*, 2021, **33**, 1–9.
3 B. E. Logan, L. Shi and R. Rossi, *Joule*, 2021, **5**, 760–762.
4 S. Dresp, F. Dionigi, M. Klingenhof and P. Strasser, *ACS Energy Lett.*, 2019, **4**, 933–942.
5 T. Liu, Z. Zhao, W. Tang, Y. Chen, C. Lan, L. Zhu, W. Jiang, Y. Wu, Y. Wang, Z. Yang, D. Yang, Q. Wang, L. Luo, T. Liu and H. Xie, *Nat. Commun.*, 2024, **15**, 1–11.
6 L. Wu, L. Yu, F. Zhang, B. McElhenny, D. Luo, A. Karim, S. Chen and Z. Ren, *Adv. Funct. Mater.*, 2021, **31**, 1–12.
7 H. Fei, R. Liu, T. Liu, M. Ju, J. Lei, Z. Wang, S. Wang, Y. Zhang, W. Chen, Z. Wu, M. Ni and J. Wang, *Adv. Mater.*, 2024, **36**, 1–29.
8 W. Tong, M. Forster, F. Dionigi, S. Dresp, R. Sadeghi Erami, P. Strasser, A. J. Cowan and P. Farràs, *Nat. Energy*, 2020, **5**, 367–377.
9 G. A. Lindquist, Q. Xu, S. Z. Oener and S. W. Boettcher, *Joule*, 2020, **4**, 2549–2561.
10 X. Ding, D. Liu, P. Zhao, X. Chen, H. Wang, F. E. Oropeza, G. Gorni, M. Barawi, M. García-Tecedor, V. A. de la Peña O'Shea, J. P. Hofmann, J. Li, J. Kim, S. Cho, R. Wu and K. H. L. Zhang, *Nat. Commun.*, 2024, **15**, 5336.
11 T. Zhang, Y. Liu, J. Yu, Q. Ye, L. Yang, Y. Li and H. J. Fan, *Adv. Mater.*, 2022, **34**, 1–9.
12 P. Zhao, Y. Zhao, H. Liang, X. Song, B. Yu, F. Liu, A. J. Ragauskas and C. Wang, *Chem. Eng. J.*, 2023, **466**, 143140.
13 S. Gupta, R. Fernandes, R. Patel, M. Spreitzer and N. Patel, *Appl. Catal., A*, 2023, **661**, 119254.
14 C. Li, Z. Wang, M. Liu, E. Wang, B. Wang, L. Xu, K. Jiang, S. Fan, Y. Sun, J. Li and K. Liu, *Nat. Commun.*, 2022, **13**, 1–11.

15 W. Han, F. Zhang, Y. He, C. Yu, L. Lei and X. Zhang, *Electrochim. Acta*, 2024, **476**, 143735.
16 J. Shi, J. Hu, Y. Luo, X. Sun and A. M. Asiri, *Catal. Sci. Technol.*, 2015, **5**, 4954–4958.
17 F. Dionigi, Z. Zeng, I. Sinev, T. Merzdorf, S. Deshpande, M. B. Lopez, S. Kunze, I. Zegkinoglou, H. Sarodnik, D. Fan, A. Bergmann, J. Drnec, J. F. de Araujo, M. Gliech, D. Teschner, J. Zhu, W. X. Li, J. Greeley, B. Roldan Cuenya and P. Strasser, *Nat. Commun.*, 2020, **11**, 1–10.
18 P. M. Bodhankar, P. B. Sarawade, G. Singh, A. Vinu and D. S. Dhawale, *J. Mater. Chem. A*, 2021, **9**, 3180–3208.
19 S. J. Huang, S. Balu, N. R. Barveen and K. S. Bayikadi, *J. Taiwan Inst. Chem. Eng.*, 2023, **152**, 105157.
20 J. Liu, Y. Ji, J. Nai, X. Niu, Y. Luo, L. Guo and S. Yang, *Energy Environ. Sci.*, 2018, **11**, 1736–1741.
21 Y. Li, L. Zhang, X. Xiang, D. Yan and F. Li, *J. Mater. Chem. A*, 2014, **2**, 13250–13258.
22 Y. Gong, H. Zhao, Y. Sun, D. Xu, D. Ye, Y. Tang, T. He and J. Zhang, *J. Colloid Interface Sci.*, 2023, **650**, 636–647.
23 Y. S. Park, J. Y. Jeong, M. J. Jang, C. Y. Kwon, G. H. Kim, J. Jeong, J. hoon Lee, J. Lee and S. M. Choi, *J. Energy Chem.*, 2022, **75**, 127–134.
24 K. Kawashima, R. A. Márquez, Y. J. Son, C. Guo, R. R. Vaidyula, L. A. Smith, C. E. Chukwuneke and C. B. Mullins, *ACS Catal.*, 2023, **13**, 1893–1898.
25 P. Chauhan, S. Siraj, K. S. Joseph, S. Dabhi, G. R. Bhadu, P. Sahatiya and C. K. Sumesh, *ACS Appl. Mater. Interfaces*, 2023, **15**, 32515–32524.
26 S. H. Hsu, C. T. Li, H. T. Chien, R. R. Salunkhe, N. Suzuki, Y. Yamauchi, K. C. Ho and K. C. W. Wu, *Sci. Rep.*, 2014, **4**, 1–6.
27 L. Chen, J. Wang, X. Shen, X. Li and C. Duan, *Inorg. Chem. Front.*, 2019, **6**, 3140–3145.
28 G. Liu, H. Zhang, J. Li, Y. Liu and M. Wang, *J. Mater. Sci.*, 2019, **54**, 9666–9678.
29 I. Ali, M. Yousaf, I. H. Sajid, M. W. Hakim and S. Rizwan, *Mater. Today Chem.*, 2023, **34**, 101766.
30 C. J. Zhang, S. Pinilla, N. McEvoy, C. P. Cullen, B. Anasori, E. Long, S. H. Park, A. Seral-Ascaso, A. Shmeliov, D. Krishnan, C. Morant, X. Liu, G. S. Duesberg, Y. Gogotsi and V. Nicolosi, *Chem. Mater.*, 2017, **29**, 4848–4856.
31 M. Wang, X. Yu, Z. Wang, X. Gong, Z. Guo and L. Dai, *J. Mater. Chem. A*, 2017, **5**, 9488–9513.
32 M. S. Faber, R. Dziedzic, M. A. Lukowski, N. S. Kaiser, Q. Ding and S. Jin, *J. Am. Chem. Soc.*, 2014, **136**, 10053–10061.
33 Q. Peng, J. Zhou, J. Chen, T. Zhang and Z. Sun, *J. Mater. Chem. A*, 2019, **7**, 26062–26070.
34 Z. Yu, Y. Li, V. Diaconescu, L. Simonelli, J. R. Esquius, I. Amorim, A. Araujo, L. Meng, J. L. Faria and L. Liu, *Adv. Funct. Mater.*, 2022, **32**, 2206138.
35 L. Yu, Q. Zhu, S. Song, B. McElhenny, D. Wang, C. Wu, Z. Qin, J. Bao, Y. Yu, S. Chen and Z. Ren, *Nat. Commun.*, 2019, **10**, 1–10.
36 M. F. Lagadec and A. Grimaud, *Nat. Mater.*, 2020, **19**, 1140–1150.
37 K. Wang, H. Du, S. He, L. Liu, K. Yang, J. Sun, Y. Liu, Z. Du, L. Xie, W. Ai and W. Huang, *Adv. Mater.*, 2021, **33**, 1–10.
38 X. Wang, M. Yang, W. Feng, L. Qiao, X. An, Q. Kong, X. Liu, Y. Wang, Y. Liu, T. Li, Z. Xiang, Q. Wang and X. Wu, *J. Electroanal. Chem.*, 2021, **903**, 115823.
39 C. Qiao, Y. Zhang, Y. Zhu, C. Cao, X. Bao and J. Xu, *J. Mater. Chem. A*, 2015, **3**, 6878–6883.
40 X. Zou, A. Goswami and T. Asefa, *J. Am. Chem. Soc.*, 2013, **135**, 17242–17245.
41 Y. Wang, S. Tao, H. Lin, G. Wang, K. Zhao, R. Cai, K. Tao, C. Zhang, M. Sun, J. Hu, B. Huang and S. Yang, *Nano Energy*, 2021, **81**, 105606.
42 E. Summary, L. Language and H. Production, *MRS Bull.*, 2023, **48**, 707–708.